

Received March 18, 2020, accepted March 26, 2020, date of publication April 1, 2020, date of current version April 23, 2020.

Digital Object Identifier 10.1109/ACCESS.2020.2984945

Research on Super-Resolution Image Reconstruction Based on Low-Resolution Infrared Sensor

YUBING LI^{1,2}, KUN ZHAO¹, FEI REN², BIAO WANG², AND JIZHONG ZHAO¹, (Member, IEEE)

¹School of Computer Science and Technology, Xi'an Jiaotong University, Xi'an 710049, China

²Research and Development Center, Changhong Meiling Company, Ltd., Hefei 230601, China

Corresponding author: Jizhong Zhao (topybl@126.com)

ABSTRACT Due to the limitation of the pixel size in the focal plane, the low-resolution(LR) infrared sensor has a very low image resolution when sampling and imaging scenes with slightly rich spatial frequencies, and aliasing is sometimes very serious. This paper uses a new technique base on sub-pixel displacement to reconstruct high-resolution(HR) images,with reduced aliasing, from a sequence of under-sampled rotated frames of the same object. First, this paper presents an image degradation model, based on the under-sampling model of the infrared image and the infrared radiation distribution on the focal plane. Second, an image reconstruction algorithm based on image micro rotation is proposed and implemented to solve the problems of inaccurate temperature measurement and target recognition caused by low resolution. Finally, the experiments results are provided to test our algorithm, and we can obtain the image whose resolution is four or five times higher than the under-sampled frames, as well as improve the temperature measurement accuracy by more than 10%. The experimental results also show that the image reconstruction algorithm is very robust, efficient and has a good reconstruction effect.


INDEX TERMS Form factor, image degradation, image reconstruction, infrared imaging, low resolution, micro-spin, super resolution.

I. INTRODUCTION

With the development of artificial intelligence technology and Internet of Things technology, IT has continued to penetrate into traditional industries, including home appliance industry. Such popularity has led to the continuous improvement of the intelligence of traditional home appliances, and home appliance intelligence has become the development trend of the home appliance industry. Interactive control has also become a hot spot of home air conditioning intellectualization in the home environment, and more and more sensors have begun to be applied, such as cameras and infrared sensors. For reasons of automatic temperature control and safety, infrared sensors have become important sensor for intelligent control of household equipment. By means of infrared sensors, the thermal image in the scene can be obtained, and the position of the human body in the hot scene can be located. Therefore, the intelligent interactive control capability and comfort level of the air conditioning will be improved. Infrared radiation (IR) technology can be used in a wide range of fields, from the military field to the general consumer

field. Moreover with development of IR imaging technology in recent years, the application field of IR imaging technology has been further expanded. Before that, IR imaging technology is the most commonly used technique in the military and national security departments. They use this technology to pre-monitor an enemy and detect/remove hidden explosives [1]. Most of these infrared devices are refrigeration infrared focal plane sensors in this field. Microsoft Kinect is the most famous typical application [2] in the civil area. It uses infrared sensors to project specific infrared point patterns onto targets and analyzes the characteristics of the point patterns to provide in-depth information and bone tracking.

Due to the Low-cost and structural requirements of the household appliance industry in applying infrared sensing, the industry mainly uses un-cooled, low-cost, low-resolution infrared array thermopile sensors. Compared with the traditional high-resolution infrared camera, the low-resolution infrared array thermopile sensor has a smaller volume and aperture, a shorter focal length, a larger pixel area, and a larger gap between the pixels. The image is very blurred, and the temperature measurement is not accurate. It is basically unable to directly meet the function needs of household appliances, especially air-conditioning products which need

The associate editor coordinating the review of this manuscript and approving it for publication was Hengyong Yu .

to obtain the object temperature, location, and orientation in the target area. Therefore, the images generated by such low-resolution sensors need to carry out super-resolution (SR) reconstruction. Super-resolution reconstruction improves the accuracy of infrared temperature telemetry while increasing the resolution to meet the needs of practical scene applications. The most common method is to use multiple low-resolution super-resolution image reconstruction techniques to achieve the above requirements.

Generally, uncooled and low-cost infrared sensors have special limitations, resulting in low resolution of infrared imaging and the high cost of obtaining high-resolution IR images. Many scholars at home and abroad have studied how to generate high-resolution or improve image resolution based on low-resolution infrared images. For example, Zhao *et al.* proposed a super-resolution infrared image reconstruction method based on sparse representation [3]. Nevertheless, there is a limit to the achievable improvement in resolution using only IR images. Meanwhile, some experts have also proposed a variety of methods to simultaneously acquire infrared images and corresponding visible light images and to fuse them in order to generate the required high-resolution infrared image [4]–[8]. For instance, Ma *et al.* proposed an IR/VIS (visible) fusion method based on gradient transfer and total variation (TV) minimization, which can keep both thermal radiation and appearance information in the source images [6]. Bavirisetti and Dululu use anisotropic diffusion to decompose a source image into approximation and detail layers, and use the Karhunen-Loeve transform (KLT) to calculate the final detail and approximation layers [7]. They produced a fused image from a linear combination of final details and approximate layers. Despite that the above two algorithms are effective in generating composite images with improved contrast, they were not developed to improve the spatial resolution of IR images. Kim and Song proposed a method of up-scaling low-resolution IR images and compositing the up-scaled images with the corresponding VIS images [8]. They first aligned the VIS image with its corresponding IR image, then, they extracted the high-frequency component information from the aligned VIS image and adaptively added it to the enlarged infrared image.

In research on image super-resolution, there are generally blurs caused by the limited detector size and optics [9], which are all described by the point spread functions, from that the degradation model and many super-resolution algorithms are obtained [10], [11]. These models and theories can be applied to many application scenarios, but they are not perfect for super-resolution applications of low-resolution IR images. First, in many applications of low-resolution infrared sensors, the range of the super-resolution is greater than the resolution of the imaging system, but can not exceed the diffraction limit of the optical system to meet the requirements. At this time, the traditional super-resolution models and algorithms are no longer suitable, and their computational complexity adds the pressure of great computational cost to

the application. Second, the super-resolution and optical blur in the traditional models are all obtained by the convolutional point spread functions of high-resolution images in obtaining low-resolution images. The large spacing between pixels in the low-resolution infrared focal plane means that the point diffusion function is no longer spatially invariant (because there are many points in the space, the Bezier peaks of their shock response all fall on the interval of the pixel [12], resulting in a small impact response). Therefore, the convolution expression in the traditional model is no longer valid. Finally, the traditional model does not consider that the energy distribution in the focal plane is the diffraction effect as well as the shape factor in the thermal radiation in the special scene of infrared imaging, [13] the related thermal image noise [14], the uncertainty of super-resolution [15], etc. The energy distribution at this time depends on the pixel field of view.

Therefore, in this paper, the irradiance distribution of point radiators with different fields of view angles on the focal plane are discussed by using the shape factor in radiometry (The results prove that the spatial translation invariance of the point diffusion function in the traditional model is invalid). The relationship between high-resolution and low-resolution images is deduced, and an image degradation model is established. A super-resolution reconstruction algorithm of multi-frame low-resolution images based on image micro-rotation is proposed, and relevant experimental demonstrations are also carried out. Because the measurement of the image motion is known, we can directly fuse low-resolution images without complex registration algorithms. At the same time, the model discussed in this article has nothing to do with specific application scenarios. The model is only related to the specific sensors used, so we can calculate the degradation matrix and store the degradation matrix in order to greatly reduce the computational requirements of the algorithm. Combined with the actual application scenario, without considering motion blur, multi-frame images (low-resolution images are not used for image reconstruction) are sampled at a fixed location and are averaged to reduce the thermal image noise. Then we use the rotation method to sample at different angles through infrared sensor, and to obtain multiple frames of low-resolution images, which, to a certain extent, solves the ill-posedness problem of super-resolution.

II. INFRARED IMAGING PRINCIPLES

The infrared sensor is very sensitive to radiation in a specific infrared band (generally, we will choose the atmospheric window). Multiple infrared sensors are integrated on a plane to form a focal plane array so that IR can be collected separately for each part of the target object. Each sensor has a readout circuit for measuring the infrared radiation energy it receives, and the value collected by each infrared sensor is converted into a grayscale value or temperature value to form an infrared image or temperature field of the target object (Fig. 1). Generally, the focal length of the infrared sensor lens is very short, and the object distance of the measured object

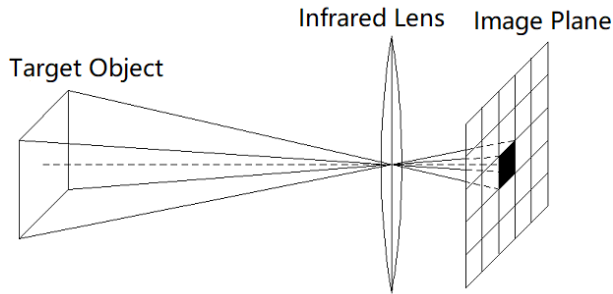


FIGURE 1. Infrared array sensor imaging.

is far greater than the focal distance. Therefore, the array is placed at the focal point of the image side of the infrared lens.

Although different types of infrared sensors have different principles, in essence, the received infrared radiation energy is converted into an electrical parameter-voltage, and the response rate of the sensor (the ratio of voltage to radiant energy), which only has a relationship with the sensor itself. Consequently, the output voltage reflects the radiant energy of the measured object. The clear relationship between radiant energy and gray is called radiation calibration, which is not necessary in an infrared measurement system without a display. For any infrared measurement system, the correction of the non-uniformity of the parameters of each sensor is essential. If the sensor has undergone radiation calibration and non-uniformity correction, the output gray value of each pixel in the focal plane is independent of the position of the pixel, but it only depends on the radiance of the object observed at the entrance pupil. The relationship between pixel gray and radiance can be expressed as follows [15]:

$$DN = aL + b, \quad (1)$$

In Equation (1), DN is the gray value of the corresponding sensor output. L is the radiance of the object observed at the entrance pupil, and a and b are fixed parameters whose values depend on the imaging system itself (such as focal length, aperture, etc.) and are irrelevant to the pixel's position in the focal plane. The position on the focal plane is irrelevant. Furthermore, according to the gray level of the image, the radiance at the entrance pupil can be calculated, and then the actual radiance of the target can be calculated from the relationship between the radiance at the entrance pupil and the original radiance of the target. Finally, the temperature of the object is calculated.

The above equation does not take into account the effects of the different emissivities of the object and the atmosphere, i.e., the gray image only reflects the brightness of the target observed at the entrance pupil. For low-resolution infrared imaging scenes and applications, we only assumed that the emissivities of various objects in the measured scene are the same (in practical applications, we always assume that the emissivity of the object we use is 0.95), and to measure

temperature in close-range, so that the above formula (1) is correct and available. The gray image obtained can still reflect the radiance distribution of the real scene to a certain extent. For example, if there is an object with low emissivity (such as glasses) in the target object, its radiance value may be also very low, and the gray value will also be very low in the radiation image, which is a ubiquitous phenomenon in the application of thermal radiation imaging, so it is not considered here.

III. THE PROPOSED METHOD

In the process of low-resolution infrared imaging and temperature measurement, due to the large pixel area, the IR from different objects or different temperature regions of the same object may be collected on one pixel, resulting in blurred images and inaccurate temperature measurement. Previously, Han *et al.* [16] proposed a convolutional neural network (CNN)-based SR algorithm to improve the resolution of near-infrared (NIR) image by combining LR IR image and HR vis image obtained simultaneously in low light environment. First, HF components are extracted from both the up-scaled version of the input LR NIR image and the corresponding HR vis image. Then the extracted heterogeneous HF image is input to CNN coupled with the auxiliary network. The two input HF features are concatenated immediately upon entering the network, and the HR HF image is synthesized through the learned convolution layer. Finally, the synthesized HR HF NIR image is added to LR NIR image to generate HR NIR image. This algorithm is also effective but it is not consistent with the actual application of our research topic. Therefore, this study uses the radiant energy distribution as well as the super-resolution model and related algorithms based on this distribution from another angle. The following explanation proves this idea in theory. The low-resolution infrared imaging is obtained by the weighted average of the gray values of high-resolution images. The gray value and the weight value depend on the imaging optical system and the position of the pixel. An algorithm that uses infrared micro-rotation to improve the resolution of the infrared image is further proposed, and to improve the accuracy of temperature measurement.

A. IRRADIANCE ILLUMINANCE DISTRIBUTION

To improve the accuracy of infrared temperature measurement, it is necessary to calculate the illumination distribution of the infrared focal plane. We assume that the infrared device is aberrated and meets the sinusoidal condition, and the oblique beam vignetting of the optical system is not considered. Then, the infrared optical lens can be approximated as an ideal optical lens, and it meets Abbe photometric law, i.e., the temperature of the target is uniform. In the case of the image, the radiance of each image point on the focal plane is the same [17] (as shown in the radiance of Q' and Q in Fig. 2), and it is proportional to the radiance of the target object. In general infrared applications, the target object is in the atmosphere, and infrared devices are evacuated due to low

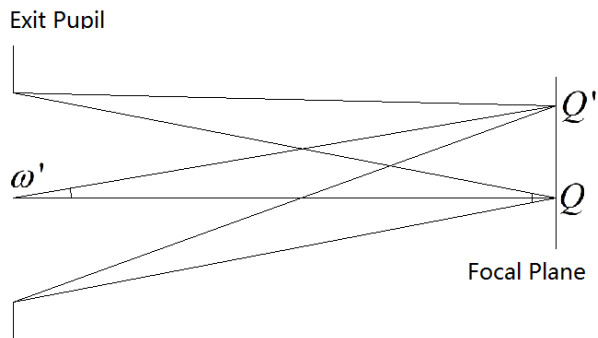


FIGURE 2. Imaging optical path of the infrared device.

thermal conductivity requirements. Therefore, the internal refractive index of the infrared device, that is, the refractive index of the image, is also close to 1. The radiation brightness of image-point [18] can be expressed in the form of Equation (2) below.

$$L' = \tau \left(\frac{n'}{n}\right)^2 L = \tau L, \tag{2}$$

In Equation (2), L' and L represent the radiance of the image point on the focal plane and the actual radiance of the target object, respectively, n' and n represent the image-side refractive index and the object-side refractive index, respectively; and τ is the transmittance of the infrared lens. We use equation (2) to calculate the radiance of the image point Q on the axis [18], and the expression is as follows.

$$E_Q = \tau \pi L \sin^2 u_0, \tag{3}$$

In Equation (3), E_Q represents the illuminance of the image point on the axis, and u_0 represents the exit aperture angle. When u_0 is relatively small, the exit pupil can be regarded as a point light source, and the radiance of the off-axis image point Q' [18] can be expressed as follows:

$$E_{Q'} = \tau \pi L \cos^4 \omega' \sin^2 u_0, \tag{4}$$

In the Equation (4), $E_{Q'}$ represents the off-axis image point illuminance, and ω' is the field angle of the off-axis image point.

In general civilian infrared systems, the infrared sensor has a simple structure and no additional aperture stop, so the actual aperture of the lens is the aperture stop. In addition, because the measured object is far away and the focal length of the lens is short, the image plane is placed at the image focal plane (this is also the reason why the infrared device is called a focal plane array), so the imaging beam angular aperture u_0 may be relatively large. The approximate conditions are not satisfied well, so it is necessary to modify the above-mentioned illumination equation (4).

In order to calculate the illuminance of the image point with a larger aperture, a more accurate calculation for the

illuminance of the off-axis image point is proposed:

$$\begin{aligned} E_{Q'} &= \int_{\Omega} \frac{\tau L \cos \theta \sin \theta d\theta d\varphi}{\cos^4 \theta (\tan^2 \theta + \sec^2 \omega' + 2 \tan \omega' \tan \theta \cos \varphi)^2} \\ &= \int_0^{u_0} \frac{\tau L \sin \theta d\theta}{\cos^3 \theta} \\ &\quad \times \int_0^{2\pi} \frac{d\varphi}{(\tan^2 \theta + \sec^2 \omega' + 2 \tan \omega' \tan \theta \cos \varphi)^2} \\ &= \frac{\tau \pi L}{2} \left(1 + \frac{\tan^2 u_0 - \sec^2 \omega'}{\sqrt{(\tan^2 u_0 + \sec^2 \omega')^2 - 4 \tan^2 \omega' \tan^2 u_0}} \right) \\ &= \tau \pi L G(Q'), \end{aligned} \tag{5}$$

Then:

$$G(Q') = \frac{1}{2} \left(1 + \frac{\tan^2 u_0 - \sec^2 \omega'}{\sqrt{(\tan^2 u_0 + \sec^2 \omega')^2 - 4 \tan^2 \omega' \tan^2 u_0}} \right), \tag{6}$$

$G(Q')$ is the form factor at the location of the image point Q' , and ω' is the field angle of the position of Q' , Ω is the integral domain, which represents the solid angle of the exit pupil relative to any point (Q') on the focal plane. $\tan^2 u_0$ can also be calculated using the optical system f/d (d is the diameter of the entrance pupil), the calculation formula is as equation (7), where fA is expressed as the aperture number.

$$\tan^2 u_0 = \left(\frac{D'/2}{f'}\right)^2 = \frac{1}{4f_A^2}, \tag{7}$$

The meaning of the parameters in the equation (7) is shown in Fig. 3. Equation (5) uses the residue theorem for the integral of φ [19].

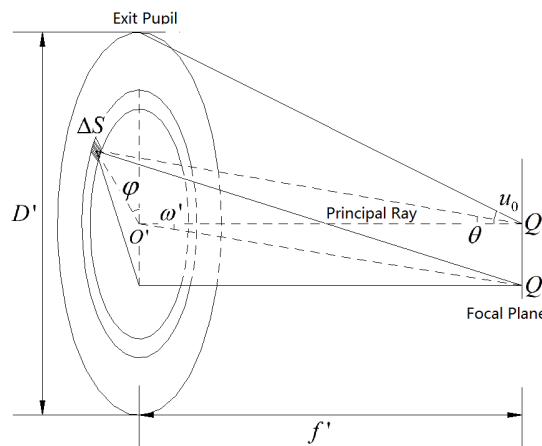


FIGURE 3. Illumination calculation for the image plane.

The significance of the equation is that, regardless of the size of the imaging beam aperture angle, as long as the aberration of the optical system is not taken into account, equation (5) can give accurate illuminance of the off-axis image point, which plays an important role in the temperature measurement and gray-scale correction of the low-resolution

infrared system. If the field angle $\omega' = 0$ in the above equation (5), the on-axis image point illuminance in equation (3) can be obtained, and then we expand the integration result as a Maclaurin series of $\tan^2 \omega'$, and the first term can be used to obtain the off-axis image point illumination in equation (4).

B. IMAGE SAMPLING MODEL

A low-resolution image is actually a down-sampling process for a high-resolution image. As shown in Fig. 4, the size of the low-resolution image is $N1 \times N2$, the pixel size is $\delta L1 \times \delta L2$, the size of the target high-resolution image is $N1L1 \times N2L2$, and the pixel size is $\delta H1 \times \delta H2$. The gap size between adjacent pixels is $\Delta 1 \times \Delta 2$ (In focal plane design, the heat conduction between pixels should be considered, so there is a certain gap between pixels.).

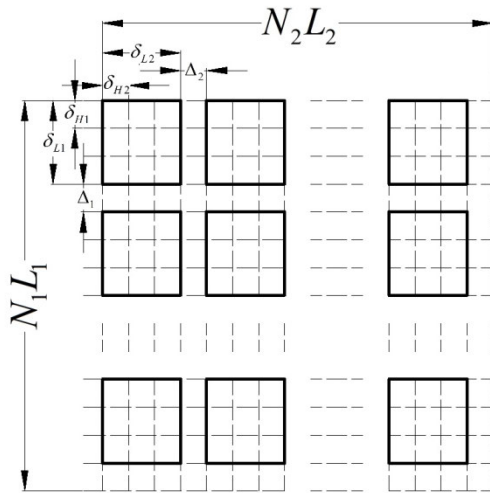


FIGURE 4. Low-resolution image sampling model.

We set the integers $m1, m2, n1$, and $n2$ satisfy the following equation(8):

$$\delta Li : \Delta i = mi : ni(i = 1, 2), \tag{8}$$

Then,we can get the following results:

$$\begin{aligned} \delta Hi &= \frac{\delta Li}{kimi} = \frac{\Delta i}{kini} \quad (i = 1, 2), \\ Li &= ki(mi + ni) \quad (i = 1, 2). \end{aligned} \tag{9}$$

In equation (9), $k1$ and $k2$ are both integers greater than or equal to 1. The larger the value of ki , the larger the multiple of the super-resolution. When ki is 1, the resolution of the super-resolution image is $N1L1 \times N2L2 = N1(m1 + n1) \times N2(m2 + n2)$. When the low-resolution infrared device is rotated slightly to the left or down by an angular displacement, a new low-resolution image is formed again.

We set the vertical and horizontal field angles of the sensor as $\theta 1$ and $\theta 2$ respectively, and the angular displacements $\Delta \theta 1$ and $\Delta \theta 2$ have the following relationship:

$$\Delta \theta i = \frac{\theta i}{NiLi} = \frac{\theta i}{Niki(mi + ni)} \quad (i = 1, 2), \tag{10}$$

For example, if a certain type of low-resolution sensor array is 24×32 , its pixel size is $60\mu m \times 75\mu m$, its pixel center distance is $100\mu m \times 100\mu m$, and its field of view is $75^\circ \times 110^\circ$. Then, $\delta L1 = 60\mu m, \delta L2=75\mu m, \Delta 1 = 40\mu m, \Delta 2 = 25\mu m, \delta L1 : \Delta 1 = 3 : 2, \delta L2 : \Delta 2 = 3 : 1$.

If we get the lowest super-resolution multiple of the low-resolution image, then $k1, k2 = 1$, so we can get $\delta H1 = 20\mu m, \delta H2 = 25\mu m$, and the size of the minimum high-resolution image is $120 \times 128, \Delta \theta 1 = 0.625^\circ, \Delta \theta 2 = 0.859^\circ$.

C. IMAGE GRAY RELATION

It is clear from the above sampling model that the output energy value of each low-resolution pixel is the algebraic sum of the energy of the high-resolution image pixels it contains. Let the pixel area of a low-resolution pixel qL be SL and the average radiance of the corresponding target part at the entrance pupil be \bar{L} . According to Equation (5), the energy ΦqL it receives can be represented as follows:

$$\Phi qL = \iint_{SL} \tau \pi \bar{L} G(\sigma) d\sigma = \tau \pi \bar{L} \iint_{SL} G(\sigma) d\sigma, \tag{11}$$

In Equation (11), σ represents an image point in SL , $d\sigma$ represents an area element containing σ , and $G(\sigma)$ is the shape factor of the area element. As mentioned earlier, $G(\sigma)$ it is related to the field angle of point σ .

Assuming that the low-resolution pixel qL contains a high-resolution pixel matrix $\{qij\}$ ($1 \leq i \leq m1, 1 \leq j \leq m2$) of $m1 \times m2$, the area of qij is SH , and the corresponding radiance of the target part at the entrance pupil is Lij . The energy ΦQij received by pixel qij is therefore expressed as follows:

$$\Phi qij = \iint_{SH} \tau \pi Lij G(\sigma) d\sigma = \tau \pi Lij \iint_{SH} G(\sigma) d\sigma, \tag{12}$$

According to the law of conservation of energy:

$$\Phi qL = \sum_{i=1}^{m1} \sum_{j=1}^{m2} \Phi qij = \tau \pi \sum_{i=1}^{m1} \sum_{j=1}^{m2} Lij \iint_{SH} G(\sigma) d\sigma, \tag{13}$$

According to equation (11) and equation(13), we can get:

$$\begin{aligned} \bar{L} &= (\sum_{i=1}^{m1} \sum_{j=1}^{m2} Lij \iint_{SH} G(\sigma) d\sigma) / (\iint_{SL} G(\sigma) d\sigma) \\ &= \sum_{i=1}^{m1} \sum_{j=1}^{m2} Kij Lij, \end{aligned} \tag{14}$$

In equation(14), Kij can be expressed as Equation (15).

$$Kij = \iint_{SH} G(\sigma) dS / \iint_{SL} G(\sigma) dS, \tag{15}$$

Because $\sum_{i=1}^{m1} \sum_{j=1}^{m2} Kij = 1$, the average radiance \bar{L} to which a low-resolution pixel can correspond is the weighted average

of the radiances of the high-resolution pixels contained in the low-resolution pixel, and the weight-factor is expressed by Equation (14). The calculation of equation (14) is relatively complicated. Because the area of the target high-resolution pixel is already sufficiently small, its internal shape factor can be approximately considered to be uniformly distributed, and it is the shape factor value of the center point of the pixel. Assuming that the area of the high-resolution pixel is D , then Equation (15) can be simplified as Equation (16):

$$\begin{aligned}
 K_{ij} &= \iint_{SH} G(\sigma) dS / \iint_{SL} G(\sigma) dS \\
 &\simeq G(\sigma_{ij}) D / \sum_{i=1}^{m_1} \sum_{j=1}^{m_2} G(\sigma_{ij}) D \\
 &= G(\sigma_{ij}) / \sum_{i=1}^{m_1} \sum_{j=1}^{m_2} G(\sigma_{ij}), \quad (16)
 \end{aligned}$$

In the above Equation (16), $G(\sigma_{ij})$ is the shape factor of the high-resolution pixel center point σ_{ij} . According to Equations (1) and (14), the grayscale of the low-resolution output image and the high-resolution image are as follows:

$$\overline{DN} = \sum_{i=1}^{m_1} \sum_{j=1}^{m_2} K_{ij} \cdot DN_{ij}, \quad (17)$$

Or:

$$\overline{DN} \sum_{i=1}^{m_1} \sum_{j=1}^{m_2} G(\sigma_{ij}) = \sum_{i=1}^{m_1} \sum_{j=1}^{m_2} G(\sigma_{ij}) \cdot DN_{ij}, \quad (18)$$

where \overline{DN} is the grayscale of the low-resolution image, and DN_{ij} is the grayscale of the high-resolution image. Equation (17) shows that the low-resolution image gray is also the weighted average of the high-resolution image gray, and the weight factor is related to the position of the corresponding high-resolution pixel. If the radiance of the target is evenly distributed, the gray level DN_{ij} of the high-resolution image does not change with the change of the pixel position. DN_{ij} in Equation (18) is therefore a constant value, so $\overline{DN} = DN_{ij}$. At the same time, because the sensor array has an ambient temperature detector, Therefore, the image gray corresponding to the ambient temperature can be replaced near the edge of the image, so in the high-resolution image reconstruction algorithm, the high-resolution image can be completely restored with the low-resolution image sequence without a difference in size.

D. IMAGE RECONSTRUCTION

The weighted average of a high-resolution image is a low-resolution image (equation 17), which is obviously a linear equation. Therefore, if there is no prior knowledge of the high-resolution image, only using a single low-resolution image will not be able to accurately restore the high-resolution image, because the number of pixels in the high-resolution image is significantly larger than that in

the low-resolution image. In this paper, we do not study the prior knowledge of high-resolution images. We only consider increasing the number of low-resolution images and performing multi-frame low-resolution image sampling. In order to make the corresponding equations of each pixel independent of each other, when we collect multi-frame low-resolution images, we need to have relative motion between these low-resolution images, and use the combination of horizontal rotation and vertical rotation to sample multi-frame low-resolution image sequences, and each rotation is the field-of-view angle of high-resolution image pixels (as shown in Table 5).

We set \overline{DN}_{ij}^{kl} ($1 \leq k \leq L1, 1 \leq l \leq L2, 1 \leq i \leq N1, 1 \leq j \leq N2$) to represent the gray scale of row i and column j in the low-resolution image of the k -th vertical direction and the l -th horizontal direction ($L1, L2, N1$, and $N2$, as mentioned above, respectively represent the super-resolution multiples of the vertical and horizontal direction and the resolution of the low-resolution image). So we can get the sub-image \overline{M}_{ij} matrix formula be as follows Equation (19):

$$\overline{M}_{ij} = \begin{bmatrix} \overline{DN}_{ij}^{11}, & \overline{DN}_{ij}^{12}, & \dots, & \overline{DN}_{ij}^{1,L_2} \\ \overline{DN}_{ij}^{21}, & \overline{DN}_{ij}^{22}, & \dots, & \overline{DN}_{ij}^{2,L_2} \\ \vdots & \vdots & & \vdots \\ \overline{DN}_{ij}^{L_1,1}, & \overline{DN}_{ij}^{L_1,2}, & \dots, & \overline{DN}_{ij}^{L_1,L_2} \end{bmatrix}_{L_1 \times L_2}, \quad (19)$$

In equation (19), $1 \leq i \leq N1, 1 \leq j \leq N2$, and then we fuse \overline{M}_{ij} into the following image \overline{Q} :

$$\overline{Q} = \begin{bmatrix} \overline{M}_{11}, & \overline{M}_{12}, & \dots, & \overline{M}_{1,N_2} \\ \overline{M}_{21}, & \overline{M}_{22}, & \dots, & \overline{M}_{2,N_2} \\ \overline{M}_{N_1,1}, & \overline{M}_{N_1,2}, & \dots, & \overline{M}_{N_1,N_2} \end{bmatrix}_{N_1 L_1 \times N_2 L_2}, \quad (20)$$

Then \overline{Q} is equal to the image of multi-frame low-rate image after registration and fusion.

We set K_{ij}^{kl} ($1 \leq k \leq m_1, 1 \leq l \leq m_2, 1 \leq i \leq N1, 1 \leq j \leq N2$) to represent the weight matrix of the i -th row and j -th column pixel of the low-resolution image, Q to represent the high-resolution image. According to the previous description, the following equation can be obtained:

$$\overline{Q}_{ij} = \sum_{k=1}^{m_1} \sum_{l=1}^{m_2} K_{[(i-1)/L_1+1],[j-1)/L_2+1]}^{kl} Q_{i+k,j+l} \quad (1 \leq i \leq N1L_1, 1 \leq j \leq N2L_2), \quad (21)$$

The square brackets in the subscript of the equation (21) indicate rounding down. In the above equation (21), the index for high-resolution image Q exceeds the limit near the boundary. therefore, we use the black body radiation brightness corresponding to the ambient temperature, and calculate the gray value by equation (1). Then we use this calculation result to fill the excess of HR image.

For Equation (21), we need to solve the unknown image \overline{Q} based on the known image Q . In this regard, both \overline{Q} and Q are expanded into a one-dimensional column vector, and the

weight matrix K is combined into a square matrix of $N_1L_1 \times N_2L_2$ according to the corresponding relationship, and then Equation (21) will be simplified to the corresponding linear equations as follows:

$$K\vec{Q}_H = \vec{Q}_L, \vec{Q}_H = K^{-1}\vec{Q}_L \quad (22)$$

In Equation (22), \vec{Q}_H represents the column vector formed by the high-resolution image Q , and \vec{Q}_L represents the column vector formed by the low-resolution image \bar{Q} . The square matrix K is a square matrix formed by weights, which is relatively large, but it is constant and sparse for certain sensors. Therefore, its inverse matrix has been stored in Flash in the application, and only matrix multiplication is executed during the calculation.

According to the above description, the algorithm steps are as follows:

Step 1: Calculate the weighting factor K of each target high-resolution pixel according to the optical system parameters of the infrared array sensor.

Step 2: Reconstitute different pixel K values into a square matrix, and calculate and store the inverse matrix K^{-1} .

Step 3: Scan the target scene horizontally and vertically to obtain a low-resolution image sequence, and regroup it to form a low-resolution registration image \bar{Q} .

Step 4: Calculate the high-resolution image Q according to Equation (22).

E. DISCUSSION

In the above algorithm, high-resolution image restoration is an image enhancement process, so the noise requirements on the input image are relatively high. If the image noise is large, the image cannot be restored at all. The inverse matrix K^{-1} is equivalent to a template for performing a deblurring operation on the low-resolution image \bar{Q} , and the processing result is sensitive to the noise of the image \bar{Q} .

At the same time, optical blur is not considered in this model. If the target resolution exceeds the limit resolution of the optical system, the degradation matrix needs to be multiplied by the optical blur factor, so the sensitivity of the algorithm to noise will be further intensified. Therefore, in the future, on the one hand, it is necessary to strengthen the research on infrared image noise models to estimate the image noise problem; on the other hand, it is necessary to further improve the algorithm, such as the fusion of deep learning methods, to further solve the ill-conditioned problem of super-resolution caused by noise.

IV. EXPERIMENT

This experiment mainly focuses on home application scenarios, especially on household appliances. Therefore, in order to better fit the practical application, we choose the uncooled infrared thermopile array sensors commonly used in the home appliance industry, which with low-cost and without display. Then, we performed a simulation experiment through an experimental turntable, and to verify the effect of the proposed

algorithm on the super resolution improvement of infrared images.

A. EXPERIMENT STEPS

The infrared sensor used in the experiment is commonly used in household appliances, which is a non-display, low-cost, non-refrigerated infrared array sensor. We named the infrared sensor used in this experiment M sensor (Fig. 5).

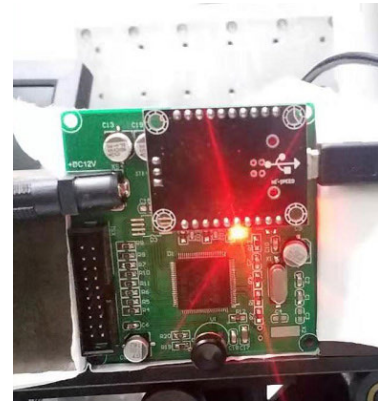


FIGURE 5. M Sensor (with driver board).

The parameters of M sensor are shown in Table 1.

TABLE 1. Parameters of M Sensor.

Parameter Name	Parameter Value
Model	M Sensor
Measuring band	$5 \mu m - 14 \mu m$
Resolving power $N_1 \times N_2$	24×32
Field angle $\theta_1 \times \theta_2$	$35^\circ \times 55^\circ$
Pixel size $\delta_{L1} \times \delta_{L2}$	$60 \mu m \times 75 \mu m$
Pixel spacing $\Delta_1 \times \Delta_2$	$40 \mu m \times 25 \mu m$
Focal length f'	3.6mm
Lens caliber D'	4.0mm

The experimental steps are as follows:

(1) Sensor calibration: Before the experiment, in order to eliminate the impact of the actual hardware environment, on the basis of the non-uniformity correction given by the manufacturer, use standard blackbody (Fig. 6) to conduct another non-uniformity correction for the sensor. Use the two-point correction method to carry out system fixed error correction for the sensor to improve the sampling accuracy. The parameters of the sensor are as follows in Table 2.

(2) Low-resolution image sampling: The sensor is placed on the experimental turntable (Fig. 7) to realize the horizontal and pitching sub-pixel displacement of two degrees of freedom and conduct sampling, the relevant parameters are shown in Table 3.



FIGURE 6. Standard blackbody.

TABLE 2. Experimental standard blackbody parameters.

Parameter Name	Parameter Value
Model	SR800-4D
Temperature range	-20°C~+80°C
Temperature accuracy	±0.015°C
Target size	100mm×100mm



FIGURE 7. Experimental turntable.

TABLE 3. Experimental turntable parameters.

Parameter Name	Parameter Value
Model	GP-500T
Pitch range	-30°~ 60°
Azimuth range	360°xN
Positioning accuracy	0.02°
Stability accuracy	0.01°

(3) Super-resolution image reconstruction: According to the above algorithm steps, the super-resolution image reconstruction is carried out. In order to determine the measurement accuracy of the temperature after super-resolution, a conventional blackbody(Fig. 8) is placed in the scene (parameters are shown in Table 4).

B. INFRARED SENSOR CALIBRATION

In order to improve the temperature measurement accuracy of the infrared sensor, a two-point calibration is performed on the sensor using a high-precision standard black body (Fig. 7). We keep the sensor close to the blackbody, so that the blackbody surface can completely cover the field of view



FIGURE 8. Conventional blackbody.

TABLE 4. Experimental conventional blackbody parameters.

Parameter Name	Parameter Value
Model	BX-350
Temperature range	-10°C~+80°C
temperature precision	±0.5°C
Target surface size	80mm

of the sensor, so that each pixel of the sensor is consistent with the target temperature, and at the same time keep a certain distance between the sensor and the target. To prevent the sensor from being affected by blackbody heat conduction. Because the practical application scene is often in the bedroom or living room of the family, we select the typical values of 25°C (air-conditioned indoor ambient temperature) and 35°C (normal human body temperature) as the reference points of the two-point correction, as the initial point and the end point respectively. (as shown in Fig. 9A and Fig. 9B).



(a)



(b)

FIGURE 9. (a) Two-point correction-blackbody temperature 25°C. (b) Two-point correction-blackbody temperature 35°C.

In the conditions of the standard blackbody settings of 25°C and 35°C, 30 frames of data are sampled, and then the 30 frames of data are arithmetically averaged at each point. The temperature measurement slope and intercept of each pixel are finally calculated.

We set T_{ij}^{25} and T_{ij}^{35} to represent the measured values of the i -th row and the j -th pixel at the standard black body at 25°C and 35°C, respectively, and we can get the following formula:

$$k_{ij} = \frac{35^\circ C - 25^\circ C}{T_{ij}^{35} - T_{ij}^{25}}, \quad b_{ij} = \frac{25^\circ C \cdot T_{ij}^{35} - 35^\circ C \cdot T_{ij}^{25}}{35^\circ C - 25^\circ C} \quad (23)$$

where k_{ij} is the slope of the two-point correction, and b_{ij} is the intercept of the two-point correction. The calibration data is shown in Figure 10. From the slope image (Fig. 10A), we can see the obvious difference between the center and edge of the sensor. This is because the pixel output voltage magnification of the edge area of the sensor’s focal plane is greater than that of the center area. At the same time, the upper left corner of the focal plane of the sensor (Fig. 10B) has a significant offset, which indicates that for the sensor, the offset calibration measures taken by the manufacturer are defective. After calibration, the relationship between the actual measurement value T_{ij}^m (Measurement) and the calibration value T_{ij}^c

(Correction) is as follows:

$$T_{ij}^c = k_{ij} \cdot T_{ij}^m + b_{ij}, \quad (24)$$

From the results above, the non-uniform characteristics of the sensor and its important effect on the temperature measurement of the infrared sensor are clear. For example, at the origin of the image, $k_{11} = 1.001$ in Fig. 10A and $b_{11} = 1.118^\circ C$ in Fig. 10B. If the measured value is $T_{11}^m = 23^\circ C$, the calibration value $T_{11}^c (=23^\circ C \times 1.001 + 1.118^\circ C = 24.141^\circ C)$ at the origin will be obtained after the correction, the error is 1.14°C. Such a large deviation has an important effect on the super resolution, so the calibration process is necessary.

C. IMAGE SAMPLING

During the experiment, we used a turntable (Fig. 6) to generate angular displacements in the azimuth (horizontal) and pitch directions. After each angular displacement, a low-resolution image was sampled to obtain a sampling sequence of low-resolution images. Before each sampling, the step value of the angular displacement must be calculated. According to formula (9), the value of ki is a positive integer. The larger the value of ki , the greater the multiple of the image super-resolution. When we set $k_1, k_2 = 1$, we can obtain the lowest multiple of the super-resolution. According to the M sensor parameters (Table 1), formula (10) is used to calculate the super-resolution experimental parameters. Table 5 shows the specific calculation experimental parameters.

When sampling, we must rotate in the horizontal direction according to the angular displacement step value of the azimuth in turn at each pitch angle, and perform a sampling after the rotation. After the horizontal sampling is completed, the first step resets the azimuth angle, the second step performs an angular displacement rotation of the elevation angle, and the third step performs horizontal rotation and sampling. Repeat these three steps to complete the sequence sampling (Figure 11A). As mentioned earlier, each sampling causes the low-resolution pixel matrix to slide horizontally or vertically across a high-resolution pixel in a high-resolution image. Figure 11B shows this oversampling process. From Table 5, in this experiment, the number of high-resolution pixels in each low-resolution pixel is $m_1 \times m_2 = 3 \times 3$, and the output gray is the weighted average of the grays of the 3×3 pixels (Equation (17)), $L_1 \times L_2 = 5 \times 4$ frames of low-resolution images need to be sampled.

The method proposed in this paper can improve the accuracy of temperature measurement, so in order to better verify this feature, we use conventional blackbody in the experimental scene. Combined with the environment of household application, the initial and final value of blackbody temperature is considered, and the blackbody temperature is set to 32°C. At the same time, our colleagues also joined the experiment to simulate the actual use of air conditioning in the environment (Fig. 12).

This experiment needs to sample a total of 20 frames of low-resolution temperature images. In order to reduce the

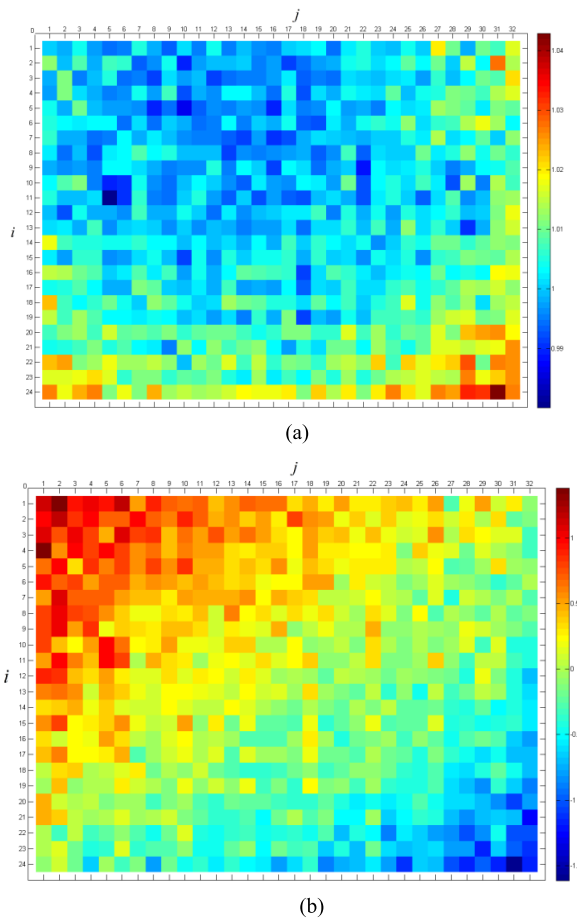
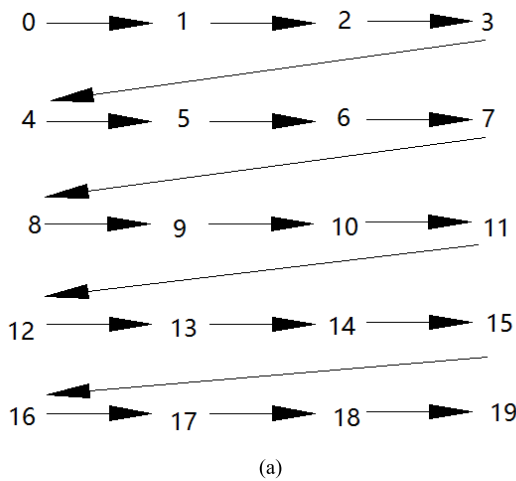


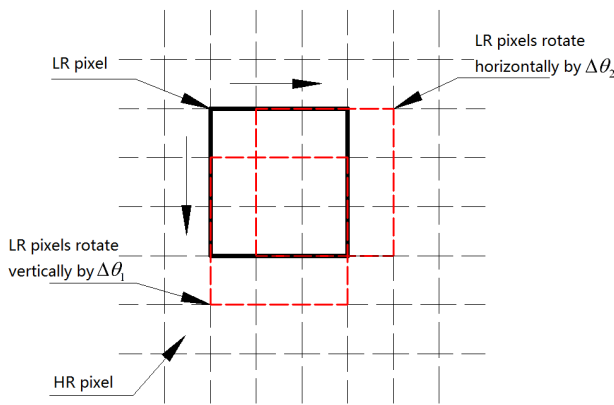
FIGURE 10. (a) Two-point correction-slope $k(i, j)$ dynamic range image. For example, the value at $k(1,1)$ is 1.001, and the value at $k(24,32)$ is 1.027. (b) Two-point correction-intercept $b(i, j)$ dynamic range image. For example, the value at $b(1,1)$ is 1.118°C, and the value at $b(24,32)$ is -1.151°C.

TABLE 5. Super-resolution experimental parameter calculation table.

Calculation Steps	Value
k_1, k_2	1 (Take the lowest super-resolution multiple)
Longitudinal clearance ratio $m_1 : n_1$	Equation (8): $m_1 : n_1 = \delta_{L1} : \Delta_1 = 60 \mu m : 40 \mu m = 3:2$
Horizontal clearance ratio $m_2 : n_2$	Equation (8): $m_2 : n_2 = \delta_{L2} : \Delta_2 = 75 \mu m : 25 \mu m = 3:1$
High-resolution cell size $\delta_{H1} \times \delta_{H2}$	Equation(9): $\delta_{H1} = \delta_{L1} / k_1 m_1 = 20 \mu m$, $\delta_{H2} = \delta_{L2} / k_2 m_2 = 25 \mu m$
Super resolution multiple $L_1 \times L_2$	Equation (9): $L_1 = k_1(m_1 + n_1) = 5$, $L_2 = k_2(m_2 + n_2) = 4$
Target high resolution $N_1 L_1 \times N_2 L_2$	$N_1 L_1 \times N_2 L_2 = 120 \times 128$
Longitudinal angular displacement $\Delta\theta_1$	Equation (10): $\Delta\theta_1 = \theta_1 / N_1 L_1 = 35^\circ / 120 = 0.292^\circ$
Horizontal angular displacement $\Delta\theta_2$	Equation (10): $\Delta\theta_2 = \theta_2 / N_2 L_2 = 55^\circ / 128 = 0.430^\circ$



(a)



(b)

FIGURE 11. (a) Low resolution image sampling sequence. (b) Low resolution pixel sampling diagram.

noise of a single frame image, we also collect 20 frames of low-resolution image data at each position and average them. Here only the first frame (Fig. 13A), the 10th frame (Fig. 13B), and the 20th frame image (Fig. 13C) are shown as examples.



FIGURE 12. Actual experimental scene.

D. RESULTS

(1) According to the abovementioned super-resolution algorithm steps, first, 20 low-resolution images need to be fused according to Equations (19) and (20). The fused low-resolution image is shown in Fig. 14A.

(2) Because the sensor gives the corrected temperature distribution directly, there is no display device, and equation (1) shows that the gray level is linear with the radiation brightness, so the coefficient $a = 1$, $b = 0$ can be set. Since the sensor outputs temperature data, the temperature needs to be converted into radiance (range 5-14um), the formula is as follows: [20]

$$L = f(T) = \eta \cdot \frac{1}{\pi} \int_5^{14} \frac{C_1}{\lambda^5} \frac{1}{e^{C_2/\lambda T}} d\lambda, \quad (25)$$

where T is the absolute temperature, η is the emissivity, C_1 and C_2 are the first and second radiation constants, and the integral variable λ is the wavelength.

The actual target radiation brightness is therefore equivalent to the gray level without affecting the experimental results. By presetting a temperature step value such as $0.1^\circ C$,

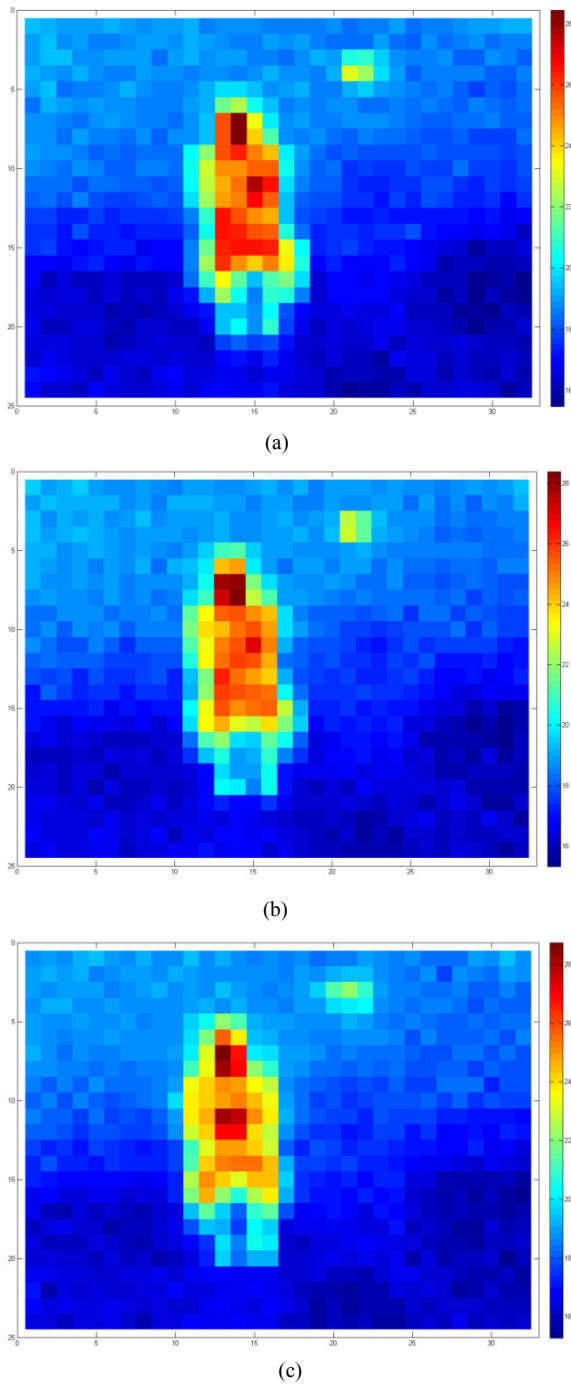


FIGURE 13. (a) The first frame of the low-resolution image. (b) The 10th frame of the low-resolution image. (c) 20th frame of the low-resolution image.

all possible measured temperature values (i.e., all radiation brightness values) are calculated in advance and are stored in Flash in the form of an array, which can easily and quickly convert the temperature image into a gray image or turn the grayscale image into a temperature image instead of real-time calculation of integration. This is done to reduce the requirements for the chip. Fig. 14B shows the result of a conversion from a temperature image to a grayscale image.

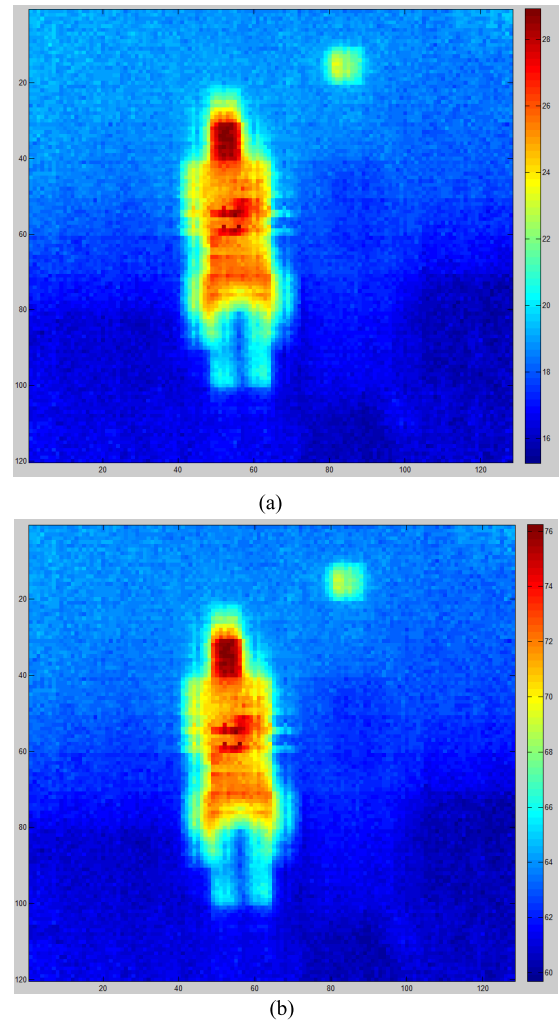


FIGURE 14. (a) Fused low-resolution image (temperature image, dynamic Range:16° C-28° C). (b) Low-resolution image after fusion (gray image, dynamic Range: 60W/(m².Sr)–76W/(m².Sr)).

(3) It has been calculated in the experiment that each low-resolution pixel contains 3×3 high-resolution pixels. According to the sensor parameters given in Table 1 and the super-resolution parameters given in Table 5, then we use formula (16) to calculate the weight matrix (i.e., degradation matrix) K (Fig. 15A). At the same time, The inverse matrix K^{-1} (Fig. 15B) is calculated in MATLAB. Although the dimension of the weight matrix is $(120 \times 128) \times (120 \times 128)$, however, from the locally enlarged image of K^{-1} shown in fig. 15C and Fig. 15D, K^{-1} is a sparse matrix and is therefore easy to store. In practical application, because K^{-1} is only related to the sensor itself and only needs to be stored, we use the formula (22), combined with the column vector \vec{Q}_L formed by the low resolution image Q to calculate the column vector \vec{Q}_H , and get the high resolution image Q .

We use the low-resolution image (Fig. 14B) and the inverse matrix of the weight matrix (Fig. 15B), and then combine formula (22) to calculate the super-resolution image. The result is shown in Fig. 16.

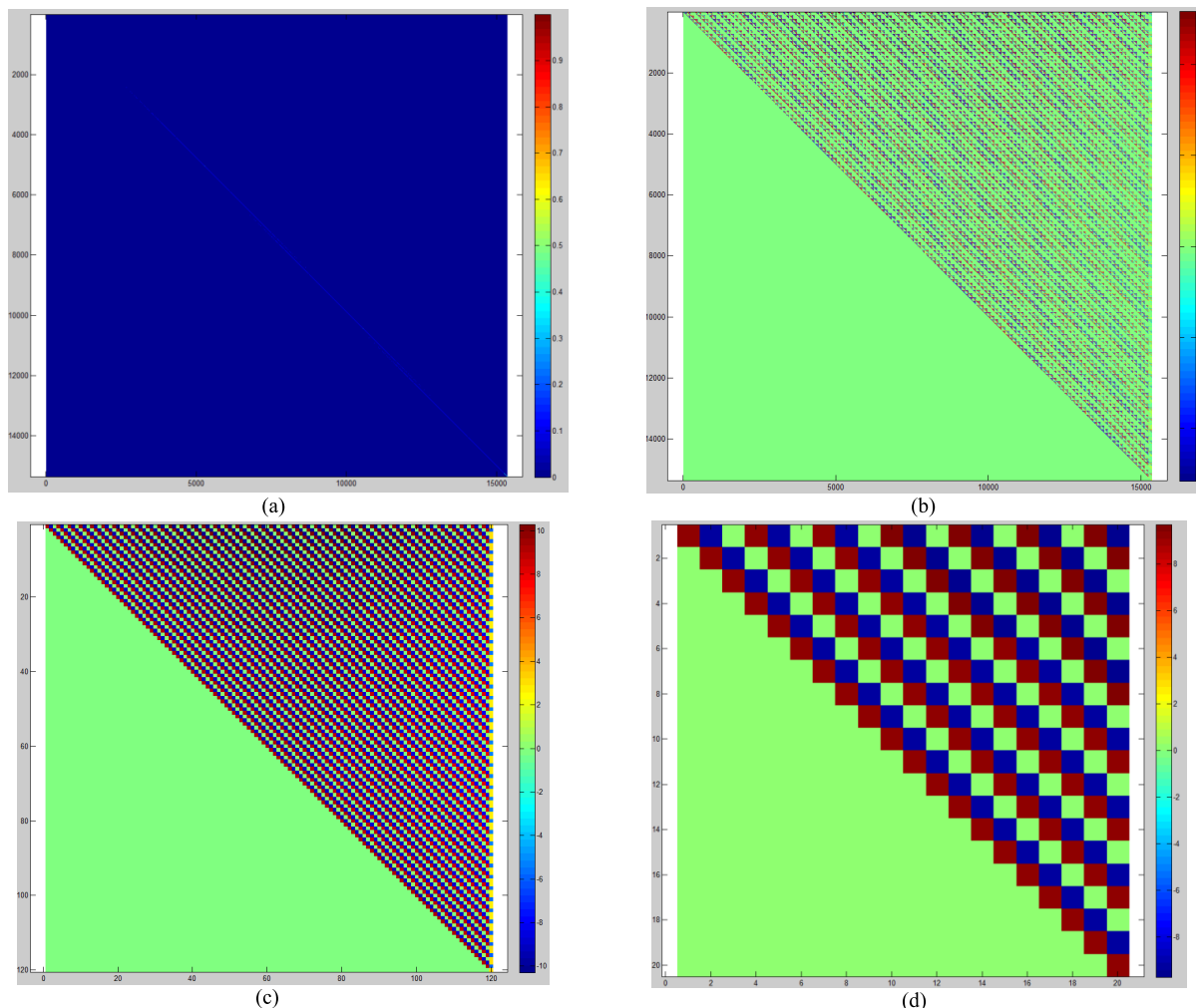


FIGURE 15. (a) Weight matrix K . (b) Weight matrix inverse matrix K . (c) Local of inverse matrix K^{-1} (1:120, 1:120) of the weight matrix. (d) Local of inverse matrix K^{-1} (1:20, 1:20) of the weight matrix.

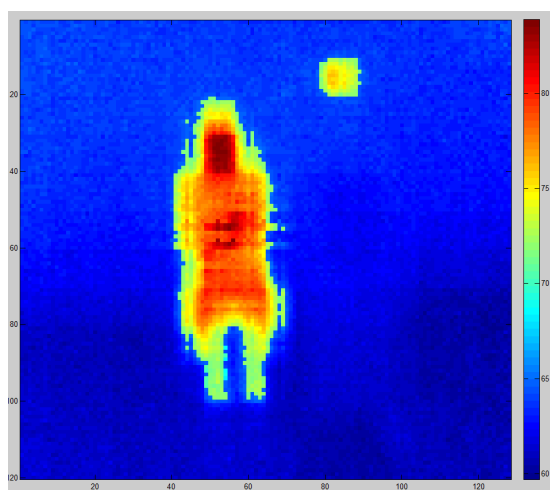


FIGURE 16. High-resolution image after reconstruction.

As shown in Fig. 16, the dynamic range of the super-resolution image (60-85) and the dynamic range of the lower-resolution image (60-76) have increased significantly.

The radiance of the human body and the black body has increased by at least 10%, while the temperature of the background does not change much, and this enhancement is particularly important in air-conditioned environments because the circulation of air can cause the objects and background to cross each other in the thermal image, and this enhancement can significantly improve the contrast of the image.

The experimental results are summarized in the following table VI:

From the experimental results in Table 6, the resolution and gray value of the test image (low-resolution image) have been significantly improved. Compared with Fig. 14B and Fig. 16, the brightness of the test image has been increased by more than 10%. The data in Table 5 further proves that the resolution of the test image has been increased by 4 times or more. At the same time, the experimental data results in Table 6 can show that the dynamic range of the image is significantly increased and the background noise is suppressed, which provides reliable original data for image recognition and application scheme based on temperature detection in the future.

TABLE 6. Comparison of experimental data.

Compare the Project	Low-Resolution Image	High-Resolution Image	Efficiency Ratio(%)
The highest radiant intensity of the human face	75.97 W/(m ² .Sr)	83.86 W/(m ² .Sr)	10.39
Maximum facial temperature	29.1°C	36.1°C	24.05
Blackbody surface radiant brightness	68.86 W/(m ² .Sr)	78.06 W/(m ² .Sr)	13.36
Blackbody surface temperature	23.1°C	30.3°C	31.17

In 2013, Tao an Yan Applied sub-pixel imaging technology in engineering projects [21]. They built an active control system for image surface displacement, and analyzed the actual image magnification through experiments. The experiment shows that for 2 times of super-resolution image, the technology actually improves the resolution multiple of low-resolution image by 1.75 times, while for 4 times of super-resolution image, the resolution of low-resolution image are increased by 2.5 times. Therefore, according to the experimental results in this paper, Image resolution and temperature measurement accuracy have been significantly improved, providing reliable raw data for subsequent image recognition and temperature-based applications, such as PMV(Predicted Mean Vote), body temperature detection, child sleep monitoring, etc.. the performance of the algorithm proposed in this paper is not lower than that of Keren algorithm and its improved algorithm based on the visible light image to improve the image resolution, but also better than the sub-pixel imaging technology to improve the image resolution (many of the previous algorithms are based on the visible light image). And because the algorithm proposed in this paper is simple and efficient, which can relatively easy to apply in household appliances with relatively weak computing power and high cost requirements.

V. CONCLUSION

Starting from the angle of the radiation intensity of illumination distribution on the focal plane and the reduced sampling model of super-resolution, our experiment theoretically proves that the weighted average of high-resolution images according to the shape factor is the low-resolution image. A super-resolution algorithm was proposed to obtain high-resolution images by an image degradation model and micro-rotation. It was confirmed through experiments that the application of this algorithm can increase the resolution of the M sensor four times, can increase the temperature measurement accuracy of the human body by 24%, and can increase the temperature measurement accuracy of the black body by 31%. Since no complicated registration algorithms and degradation factors are required and the application scenarios do not change, the complexity of the algorithm is very

low, thus providing the possibility for embedded applications of this model and algorithm.

During the experiment, the method adopted is to use the two-point correction of the black body to reduce the fixed error caused by the sensor and use the average value of multiple frames of images to eliminate the random error of the infrared measurement,, which played a key role in the success of the experiment, and the stationary or low-speed movement of a hot target also works very well. The significance of the model in practical applications as follows: First, it provides a learning model for a CNN (Convolutional Neural Network) super-resolution algorithm that implements a single-frame image in the cloud. The second is to enrich the degradation model in the image super-resolution reconstruction theory, which is conducive to improving the effect of image super-resolution, especially in applications based on low-resolution infrared sensor imaging and temperature measurement.

The algorithm proposed in this paper can not only make the low-cost and low-resolution infrared thermopile sensor meet the needs of scene application in the home environment, but also enable the device installed with the sensor to realize the ability of active perception of people, especially for the application of low resolution infrared technique is very effective, which shows that the research results of this paper have a certain popularity.

As artificial intelligence technology continues to promote the intelligent transformation of white goods and related home products, and it continuously improves the level of product intelligence, people continue to raise the requirements for the quality of family life. In the home environment, the requirements for security and privacy are also further increased. The change of consumption concept also provides opportunities for the popularity of infrared sensor devices in the field of consumption.

REFERENCES

- [1] K. H. Ghazali and M. S. Jadin, "Detection improvised explosive device (IED) emplacement using infrared image," in *Proc. UKSim-AMSS 16th Int. Conf. Comput. Model. Simulation*, Mar. 2014, pp. 307–310.
- [2] Z. Zhang, "Microsoft kinect sensor and its effect," *IEEE Multimedia Mag.*, vol. 19, no. 2, pp. 4–10, Feb. 2012.
- [3] Y. Zhao, Q. Chen, X. Sui, and G. Gu, "A novel infrared image super-resolution method based on sparse representation," *Infr. Phys. Technol.*, vol. 71, pp. 506–513, Jul. 2015.
- [4] X. Li and S.-Y. Qin, "Efficient fusion for infrared and visible images based on compressive sensing principle," *IET Image Process.*, vol. 5, no. 2, pp. 141–147, 2011.
- [5] A. Gyaourova, G. Bebis, and I. Pavlidis, "Fusion of infrared and visible images for face recognition," in *Proc. Eur. Conf. Comput. Vis. (ECCV)*, 2004, pp. 456–468.
- [6] J. Ma, C. Chen, C. Li, and J. Huang, "Infrared and visible image fusion via gradient transfer and total variation minimization," *Inf. Fusion*, vol. 31, pp. 100–109, Sep. 2016.
- [7] D. P. Bavirisetti and R. Dhuli, "Fusion of infrared and visible sensor images based on anisotropic diffusion and Karhunen–Loeve transform," *IEEE Sensors J.*, vol. 16, no. 1, pp. 203–209, Jan. 2016.
- [8] Y. J. Kim and B. C. Song, "Infrared image sharpness enhancement method using super-resolution based on adaptive dynamic range coding and fusion with visible image," *J. Inst. Electron. Inf. Eng.*, vol. 53, no. 11, pp. 73–81, Nov. 2016.
- [9] F. Zhou, "A review of super-resolution image restoration," *Automat. Instrum.*, vol. 1, pp. 10–14, 2006.

[10] M. Irani and S. Peleg, "Super resolution from image sequences," in *Proc. 10th Int. Conf. Pattern Recognit.*, 1990, pp. 115–120.

[11] H. Stark and P. Oskoui, "High-resolution image recovery from image-plane arrays, using convex projections," *J. Opt. Soc. Amer. A, Opt. Image Sci.*, vol. 6, no. 11, pp. 1715–1726, 1989.

[12] J. W. Goodman, *Introduction to Fourier Optics*, 3rd ed. Beijing, China: Electronic Industry Press, 2016.

[13] J. Q. Zhang, *Infrared Physics*, 2nd ed. Xi'an, China: Xidian Univ. Press, 2013.

[14] B. Chang and Y. Cai, *Infrared Imaging Array and System*. Beijing, China: Science Press, 2006.

[15] J. Hadamard, *Lectures on Cauchy's Problem in Linear Partial Differential Equations*. Beijing, China: Higher Education Press, 2016.

[16] T. Y. Han, D. H. Kim, S. H. Lee, and B. C. Song, "Infrared image super-resolution using auxiliary convolutional neural network and visible image under low-light conditions," *J. Vis. Commun. Image Represent.*, vol. 51, pp. 191–200, Feb. 2018.

[17] L. H. Cao, N. Li, C. Y. Yang, L. H. Guo, and G. L. Si, "Radiance calibration for 3-5 μm infrared detector," *Infr. Laser Eng.*, vol. 41, no. 4, pp. 858–864, 2012.

[18] M. Born and E. Wolf, "Principles of optics-electromagnetic theory of propagation," in *Interference and Diffraction of Light*, 7th ed. Beijing, China: Electronics Industry Press, 2016.

[19] Q. Q. Fang, *Complex Function Tutorial*. Beijing, China: Peking Univ. Press, 2017.

[20] Z. D. Chu and Y. J. Wang, *Theory and Engineering Practice of IR Heating Drying*. Beijing, China: Chemical Industry Press, 2019.

[21] X. T. Xiaoping Tao and F. Y. Feng Yan, "Image improvement based on sub-pixel post-integration for a staring imaging system in geostationary orbit," *Chin. Opt. Lett.*, vol. 12, no. 4, pp. 042802–42806, 2014.



KUN ZHAO received the Ph.D. degree in computer science from Xi'an Jiaotong University, Xi'an, China. He is currently an Assistant Professor with Xi'an Jiaotong University. His research interests include mobile computing, wireless security, and federated learning.



FEI REN received the M.S. degree in software engineering and the Ph.D. degree in information and communication engineering from the University of Electronic Science and Technology of China (UESTC), in 2006 and 2013, respectively. He is currently a Senior Engineer with Changhong Meiling Company, Ltd. His research interests include information security, trusted distributed networks, the IoT, and image recognition.



BIAO WANG received the B.S. degree in electronic information science and technology from the Qingdao University of Technology, with a minor in applied physics. His research interests include image recognition, image processing, and optics.



YUBING LI is currently pursuing the Ph.D. degree with the School of Computer Science and Technology, Xi'an Jiaotong University (XJTU). He was responsible for intelligent technology research and development, the frequency conversion technology research and development, product innovation, and management work of Changhong Meiling Company, Ltd., China. He is currently a Senior Engineer with XJTU. His research interests include the IoT, Image recognition, deep learning, and intelligent control.



JIZHONG ZHAO (Member, IEEE) is currently a Professor with the School of Computer Science and Technology, Xi'an Jiaotong University. His research interests include pervasive computing, the IoT, network security, and deep learning. He is a member of CCF and ACM.

...